Clustering reveals cavitation-related acoustic emission signals from dehydrating branches

Lidewei L. Vergeynst[1], Markus G.R. Sause[2], Niels J.F. De Baerdemaeker[1], Linus De Roo[1] and Kathy Steppe[1,3]

[1]Laboratory of Plant Ecology, Department of Applied Ecology and Environmental Biology, Faculty of Bioscience Engineering, Ghent University, Coupure Links 653, B-9000 Ghent, Belgium; [2]Experimental Physics II, Institute for Physics, University of Augsburg, D-86135 Augsburg, Germany; [3]Corresponding author (kathy.steppe@ugent.be)

The formation of air emboli in the xylem during drought is one of the key processes leading to plant mortality due to loss in hydraulic conductivity, and strongly fuels the interest in quantifying vulnerability to cavitation. The acoustic emission (AE) technique can be used to measure hydraulic conductivity losses and construct vulnerability curves. For years, it has been believed that all the AE signals are produced by the formation of gas emboli in the xylem sap under tension. More recent experiments, however, demonstrate that gas emboli formation cannot explain all the signals detected during drought, suggesting that different sources of AE exist. This complicates the use of the AE technique to measure emboli formation in plants. We therefore analysed AE waveforms measured on branches of grapevine (*Vitis vinifera* L. 'Chardonnay') during bench dehydration with broadband sensors, and applied an automated clustering algorithm in order to find natural clusters of AE signals. We used AE features and AE activity patterns during consecutive dehydration phases to identify the different AE sources. Based on the frequency spectrum of the signals, we distinguished three different types of AE signals, of which the frequency cluster with high 100–200 kHz frequency content was strongly correlated with cavitation. Our results indicate that cavitation-related AE signals can be filtered from other AE sources, which presents a promising avenue into quantifying xylem embolism in plants in laboratory and field conditions.

Introduction

Plant survival during drought is of increasing interest in plant science. We need accurate quantification of the vulnerability to drought, not only for predicting plant responses to a changing climate but also as a tool to select and breed suitable, drought-tolerant plants for production. Vulnerability to air emboli formation in sap-conducting elements is one of the key features in this context (Lens et al. 2013, Carevic et al. 2014, Delzon and Cochard 2014). The formation of air emboli, also called cavitation because air bubbles are formed in the sap under tension, reduces the plant's hydraulic conductivity and impedes the manifold vital functions of sap transport in plants. Several techniques (Cochard et al. 2013) have been developed to quantify vulnerability to cavitation, based on the reduction in hydraulic conductivity with respect to increasing xylem tension. Acoustic emission (AE) sensors can be used to measure the loss in hydraulic conductivity (Vergeynst et al. 2015*a*). The AE technique is gaining renewed attention (Rosner 2015) because it is non-destructive and can be applied without cutting the xylem conduits open, a process which is currently facing a barrage of criticism because of the risk of artificial embolisms when using the hydraulic method (McElrone et al. 2012, Sperry 2013, Martin-StPaul et al. 2014, Torres-Ruiz et al. 2015).

Despite the practical advantages of the AE technique, being automatic and less labour intensive compared with other known techniques, the indirect measurement of hydraulic conductivity loss is considered a major drawback. The actual nature of the AE

signals, and thus their link with hydraulic conductivity loss, is not fully understood, questioning the belief that all AEs originate from gas emboli formation (Tyree and Dixon 1983). It has been demonstrated that cavitation in xylem conduits induces a pressure wave that is detectable with AE sensors (Ponomarenko et al. 2014) in dehydrating microscopic xylem slices of the gymnosperm *Pinus sylvestris* L. However, when measuring on larger samples (Rosner et al. 2006) or whole branches (Vergeynst et al. 2015*a*), the number of measured AE signals may largely exceed the number of xylem conduits. Also, AE activity is observed to continue beyond the point of 100% loss of conductivity (Wolkerstorfer et al. 2012, Vergeynst et al. 2015*a*). This implies that cavitation cannot explain all detected AE signals, and that most likely other sources of drying-induced AE signals exist. To become confident in the use of the AE technique for measuring hydraulic conductivity loss, it is imperative for us to elucidate the different sources that produce AE signals in drought-stressed plants.

If different AE sources are active, they should be distinguished based on the waveforms of the detected AE signals (Sause 2010, Aggelis et al. 2013). Therefore, in this research, we recorded whole waveforms of AE signals from dehydrating grapevine branches (*Vitis vinifera* L. 'Chardonnay') with broadband point-contact sensors. We searched for different types of AE signals using an automated clustering algorithm based on a set of seven frequency features. During branch dehydration, we also recorded diameter shrinkage, gravimetric water loss and xylem water potential. In this article, we explain the meaning of different types of AE signals by relating their activity to the different phases observed during bench dehydration as given by the acoustic vulnerability curve (VC) (Vergeynst et al. 2015*a*).

Materials and methods

Measurements during branch dehydration

Plant material was collected in September 2014 from fruit-bearing wood of grapevine (*V. vinifera* L. 'Chardonnay') in a vineyard located in Lede, Belgium (50°57′57″N, 3°58′39″E). The day before cutting the branches, the leaves of three branches of ~100 cm length and 7.5 ± 1.1 mm diameter were packed in aluminium foil. A broadband point-contact AE sensor (KRNBB-PC, KRN Services, Richland, WA, USA) and a holder for the diameter dendrometer (DD-S, Ecomatik, Dachau, Germany) were installed on the branches at distances of ~30 and ~22 cm, respectively, from the top of the branch. Use of a broadband point-contact AE sensor was needed for this experiment, because of its flat spectral response in the frequency range 20–1000 kHz (Sause et al. 2012*b*), which makes this sensor most appropriate to experimentally verify simulated signals (Vergeynst et al. 2015*b*). The AE sensor was pressed to the branch surface using a compression spring (D22050, Tevema, Amsterdam, The Netherlands) in a small PVC tube. A droplet of vacuum grease (High-Vacuum Grease, Dow Corning, Seneffe, Belgium) was applied between sensor tip and wood to ensure good acoustic contact. The next day, before sunrise, the three branches were excised under water and the cut surface was kept under water in plastic test tubes. Packed in an opaque plastic bag, the branches were transported to the laboratory. In the laboratory, the dendrometers were installed after removing the bark at the dendrometer contact area with a scalpel and smearing with petroleum jelly to prevent direct evaporation through the wound.

We cut a piece of ~40 cm at the lower side of each branch and placed it on an electronic balance (2× DK 6200 and 1× PS 4500/C/1, Henk Maas, Veen, The Netherlands), stripped of all leaves. The wounds of the cut petioles were covered with petroleum jelly (Vaseline). A wood sample of ~4 cm was taken from the cut end of the other branch part. Also, after the 4.5-day dehydration period, a wood sample was taken from the middle of both branch parts. We determined the volumetric water content (VWC, kg m^{-3}) of the samples and used these measurements, together with the continuous measurements of the balance, to calculate continuous VWC throughout the dehydration period (details of the method in Vergeynst et al. 2015*a*).

Every 3 h, we measured xylem water potential (ψ, MPa) on an excised leaf with the pressure bomb (PMS Instrument Company, Corvalis, OR, USA). We determined the linear stress–strain relationship (Irvine and Grace 1997, Vergeynst et al. 2015*a*) for each branch and calculated continuous xylem water potential as described by Vergeynst et al. (2015*a*).

The dendrometers and the electronic balances were read out each minute using custom-built acquisition boards. The AE signals were amplified by 35.6 dB (AMP-1BB-J, KRN Services) and waveforms of 7168 samples length were acquired at 10 MHz sample rate. An electronic bandpass filter of 20–1000 kHz was applied and all waveforms above the noise level of 28 dB_{AE} were collected.

Feature extraction and automated clustering algorithm

To investigate the presence of different AE sources, we first grouped the signals based on similarity of their frequency features using an automated clustering algorithm as described in detail in Sause et al. (2012*a*). A flow chart of this clustering algorithm, adapted for our specific application, is shown in Figure 1. To this end, a set of seven frequency features and four waveform features were calculated for each waveform in the software NOESIS (Envirocoustics S.A., Athens, Greece). These features were chosen because each of them contains different information about the AE source, and the more information that is incorporated in this analysis, the larger the chance is of finding specific features that can be linked to cavitation as an AE source. Feature extraction was conducted on the initial 50 µs after the time of arrival (500 samples) and frequencies below 50 kHz were filtered with an eighth order Butterworth filter. The following waveform features were calculated: amplitude (dB), rise time

(µs), rise angle (rad) (Figure 2) and absolute energy (aJ) (Sause 2010). From the frequency spectrum (Figure 2), we extracted peak frequency (PF), frequency centroid (FC), weighted PF (WPF, geometric mean of PF and FC) and the partial powers of the following frequency ranges: 0–100, 100–200, 200–400 and 400–800 kHz (PP1–4) (Sause 2010). We then screened the dataset for the presence of two to four clusters using each possible combination of four to seven frequency features (Figure 1). The algorithm gives as output the ranking of the 192 clustering results (64 features combinations × 3 numbers of clusters) according to four cluster indices: the Tou-index, Rousseeuw's silhouette value, the Pearson's Gamma statistic and the Davies–Bouldin index. For each cluster index, the 25 best partitions get a score of 25–1, and the partitions are ordered according to the sum of the four scores. Because the calculation of the cluster indices is computationally intensive for very large datasets (in our case in the order of magnitude of 10^5 AE signals), we used for each of the 64 feature combinations a new random sample of 4000 AE signals from all signals collected in the three branches and a pooled analysis was done where data of all three branches were put together. Data analysis and graphical display were performed using the R software (R version 3.0.1; R Development Core Team 2013). Next, we investigated whether these natural clusters or signal types belong to a certain physiological process during dehydration.

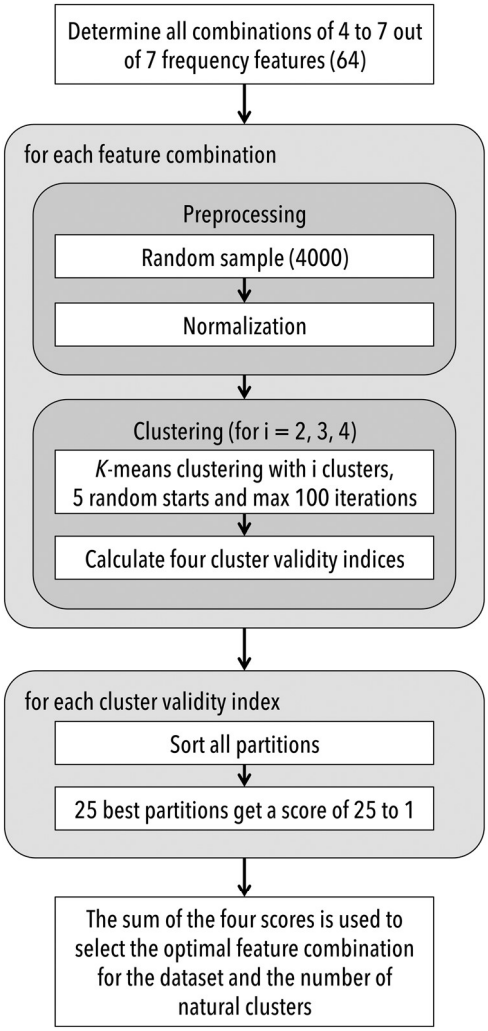

Figure 1. The amount of natural clusters and the optimal feature combination using an automated clustering algorithm. The flow chart of Sause et al. (2012*a*) is adapted here for our specific application.

The same analysis with feature extraction and automated clustering was also performed on the AE data obtained during the dehydration experiment described in Vergeynst et al. (2015*a*). In this experiment, we used two broadband point-contact sensors to monitor AE activity during 40 h dehydration of a grapevine branch simultaneous with continuous visualization of cavitated vessels using micro-computed tomography (µCT). The two sensors were installed at 2 cm (upper sensor) and 16 cm (lower sensor) distance from the scanned zone in the middle of the branch.

End point of the acoustic VC and transition between elastic shrinkage and cavitation

For each of the obtained clusters and for all the AE signals together, we constructed an acoustic VC in order to compare the appearance of the clusters with other plant physiological measurements. For the calculation of the characteristic points of the curves, the end points were defined by the end of the AE activity peaks. We determined the end point of the curves as the point at which the decrease in AE activity, following the AE activity

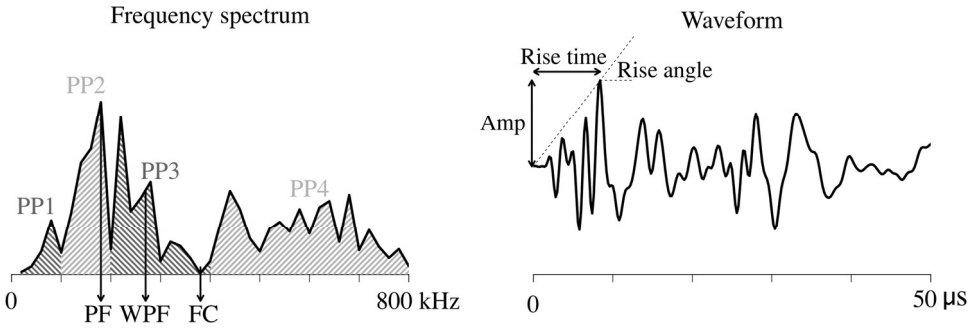

Figure 2. Frequency features PF, WPF, FC and four partial powers (PP1–4) were used for the automated clustering algorithm. Waveform features rise time, amplitude and rise angle describe the shape of the AE signal.

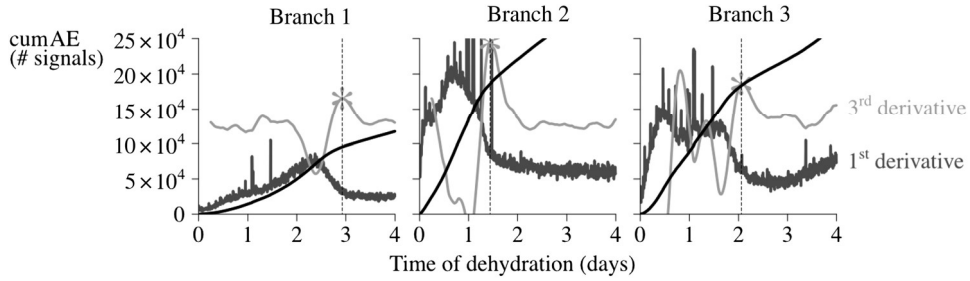

Figure 3. We calculated the point of 100% loss of hydraulic conductivity as the end point of the AE activity (first derivative of the curve of cumulative AE) peak, where the third derivative of the curve of cumulative AE signals in time reached a local maximum, as indicated by the vertical dashed line. Here, the curves of total AE are shown. The recorded spikes in the AE activity of Branch 2 are probably due to background noise (e.g., from cutting the leaves for water potential measurements) but do not influence the cumulative AE as they are negligible compared with the other signals and are therefore not completely shown.

peak, decreased most strongly. Mathematically, this point can be found where the third derivative of the curve of cumulative AE versus time reaches a local maximum (Figure 3). The AE activity (first derivative) was calculated numerically over a time interval of 15 min, while a time interval of 12 h was used for the second and third derivatives. The longer interval was chosen in order to eliminate the strong small-scale fluctuations of the first derivative and was based on the timescale at which the AE peak occurred. When dehydration occurs much faster, in different samples or under different conditions, this time interval may be adapted in order to obtain meaningful results. The recorded spikes in AE activity were attributed to noise but did not influence the cumulative AE as they were negligible compared with the other signals (Figure 3). For the transition point between the elastic shrinkage and the cavitation phase, we searched for a minimum in the second derivative to the curve of VWC versus water potential. This is the point where the hydraulic capacitance (first derivative to the curve) increased most strongly. The elastic shrinkage phase is characterized by few cavitation events and a strong diameter contraction (Vergeynst et al. 2015*a*).

Results

Clustering of AE signals reveals three clusters

A first application of the automated clustering algorithm (Figure 1) suggested an optimal clustering based on the frequency features (Figure 2) FC, PF, WPF and partial power in the range 400–800 kHz (PP4) (Figure 4a and b; Table 1). The clustering resulted in a small partition containing signals with high PP4 and high WPF. The other cluster contained 98–99% of all signals and showed a large variation in the frequency range 100–200 kHz. A second clustering of this predominating cluster resulted in a third cluster (Figure 4c and d; Table 1), based on the frequency features PF, WPF and partial powers in the frequency ranges 0–100 kHz (PP1) and 100–200 kHz (PP2). Based on their frequency content, the three clusters were labelled as the low-, mid- and high-frequency clusters. High PP1 and PP2 were typical for the low- and mid-frequency clusters, respectively (Figure 5). The high-frequency cluster was characterized by a high PP4, PF, FC and WPF. These signals were slightly larger in amplitude and had a shorter rise time, resulting in the largest rise angles. The low-frequency cluster also contained signals with small rise time, but from the violin plots (Figure 5), it is clear that a large portion has longer rise times and small rise angles. The average absolute energy was highest for the low-frequency cluster and lowest for the mid-frequency cluster.

Vulnerability curves

The VC developed with all AE signals (Figure 6a) contained an initial shrinkage phase, followed by a cavitation phase with higher capacitance (Figure 6b; Table 2). The VCs based on the low- and mid-frequency clusters (Figure 6c; Table 3) were quite similar to the curve that included all AE signals. However, the activity of the low-frequency cluster remained high after the end point of the curve (Figure 6d), whereas the activity of the mid-frequency cluster reached almost zero. The high-frequency cluster, in contrast, was mainly active during the elastic shrinkage phase with fast shrinkage (Figure 6e), and reached its end point far before the two other clusters.

Validation with µCT

The AE signals from the grapevine branch in the µCT experiment contained the same three clusters. The high-frequency signal type showed a strong activity at the beginning of dehydration (Figure 7), while mid-frequency and, especially, low-frequency signal types showed a better correlation with the number of emptied vessels.

Discussion

Vulnerability curves based on AE activity peak

Defining the end point of the cavitation phase, when percentage loss of conductivity (PLC) reaches 100%, is crucial to the development of meaningful acoustic VCs, but has always been a main difficulty with the AE technique, particularly in angiosperms (Rosner 2015). Ideally, PLC should by definition be only linked

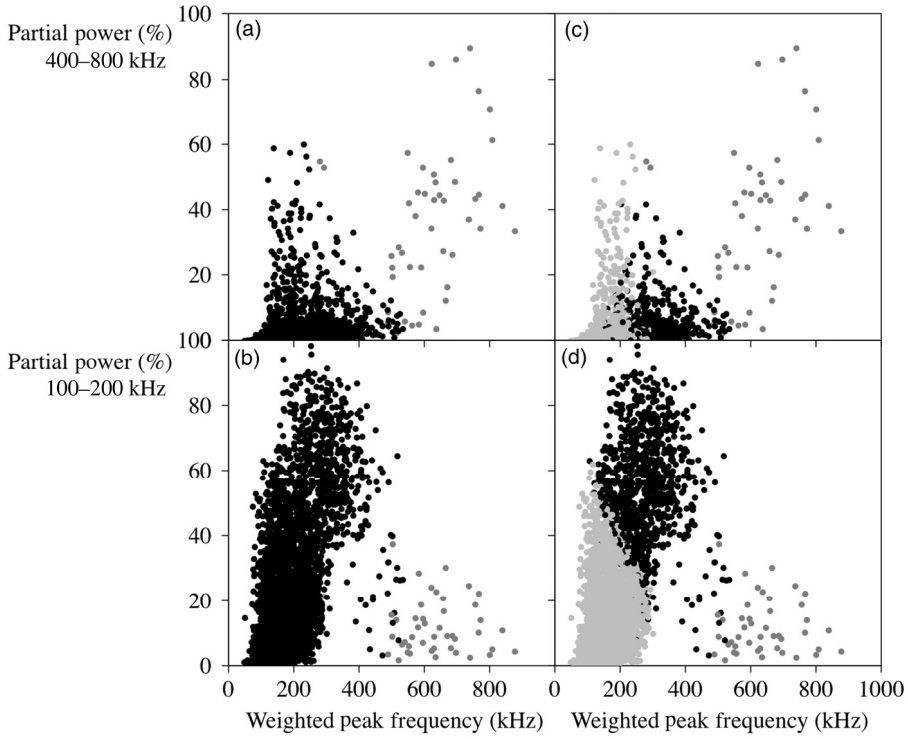

Figure 4. The first clustering of the whole dataset (all AE signals from three branches) resulted in two clusters (a and b). When removing the high-frequency cluster (grey) from the dataset, a second clustering split the lower-frequency cluster into the low-frequency (light grey) and mid-frequency (black) clusters (c and d).

Table 1. The cluster indices are a measure of the clustering quality. The second clustering is based on the data from the lowest frequency cluster that resulted from the first clustering.

	Davies–Bouldin index	Tou-index	Rousseeuw's silhouette value	Pearson's Gamma statistic
First clustering	0.564	2.568	0.786	0.746
Second clustering	0.784	2.032	0.594	0.752

to cumulative AE and according to Aggelis et al. (2010), a specific AE-inducing mechanism results in an AE activity. Therefore, in contrast to our previous work (Vergeynst et al. 2015*a*), the end point of the VC is now determined by the behaviour of the AE activity peak and its return to zero, and corresponds to the local maximum of the third derivative of the curve of cumulative AE versus time (Figure 3). This makes it possible to define a clear end point, even in situations where the VC does not clearly level off due to strong decrease in diameter shrinkage, e.g., for Branch 3 in Figure 6a, and also when continuous measurements of water potential are not available.

The difficulty in determining the end point of VCs based on AEs has also been addressed by Nolf et al. (2015). To tackle this problem, the authors hypothesized that the highest acoustic activity should occur near the steepest part of the VC, which is the inflection point, reflecting P_{50}. They obtained good similarity when comparing their method with hydraulic measurements of 16 species, although P_{50} in angiosperms derived from AE measurements was consistently slightly overestimated (i.e., more negative). The major drawback of this approach is the requirement of a VC that is perfectly sigmoidal S-shaped. A deviation from this ideal curve causes the steepest part to deviate from the targeted P_{50} value, which implies that using maximum AE activity in practical applications might not always be a good measure for P_{50}. An origin-based selection of AE, like clustering, should be done first to make sure that the considered AE activity is correlated to cavitation activity before conclusions can be made.

Transition between elastic shrinkage and cavitation (Figure 6b) delimits two phases with different hydraulic capacitance. We therefore consider it most meaningful to define the transition at the point where the capacitance changes most strongly. We calculated the point of the dehydration curve where the hydraulic capacitance increased most strongly, instead of taking the average of the breakpoints of both curves as defined in Vergeynst et al. (2015*a*). The re-definition of the end points does not alter results previously presented, but we propose to use these new definitions because they have a physiological meaning.

Although the curve of total cumulative AE signals resulted in plausible values for P_{50} (–2.30 to –2.73 MPa; Table 3) when compared with other methods (–2.17 to –2.97 MPa; Choat et al. 2010, Brodersen et al. 2013), the total AE activity continued

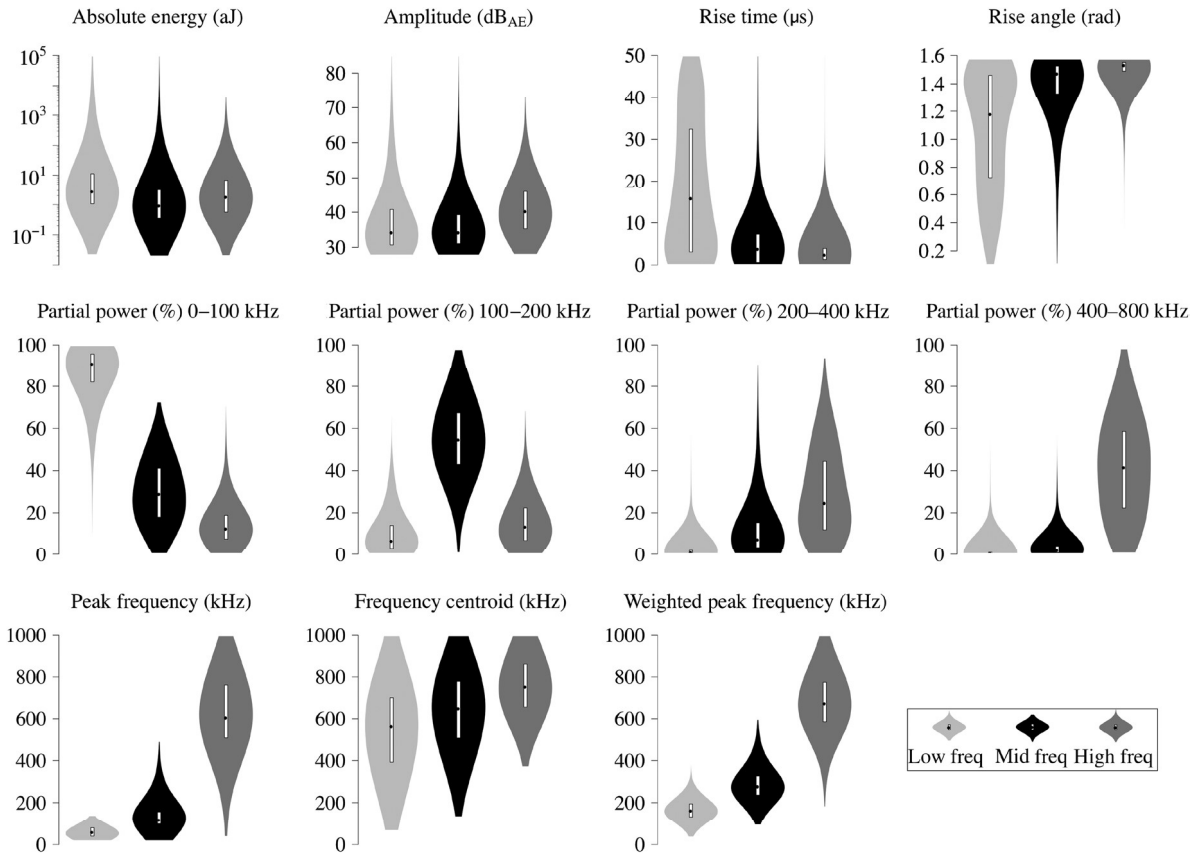

Figure 5. The distributions of the signal features for the three frequency clusters (low, mid and high) are visualized by vioplots (Adler 2005). The box plot indicates the lower hinge, the median and the upper hinge. Overlaid on this box is a violin plot, showing the distribution of the data using the kernel density estimation.

beyond 100% PLC (Figures 3 and 6a). Acoustic emission sources that were not related to cavitation most likely caused this additional AE activity. We aimed at filtering out these different AE sources by searching for natural clusters in the AE signals. Waveform features, which are generally used in cavitation research in conifers (Rosner et al. 2006), did not result in a good clustering as there was too much overlap between the three clusters (Figure 5). For composite materials, which also include the natural composite wood (Baensch et al. 2015), frequency features have been proven to be useful for identification of different AE sources (Sause and Horn 2010). Our observation of three different clusters of AE signals during dehydration of the branches strongly suggested the presence of at least three types of AE sources. The activity of the mid-frequency cluster became almost zero at the VC end point (Figure 6d). This AE signal type was thus better related to the expected definition of emboli formation in the xylem than the low-frequency cluster, with continued activity after the end point, and the high-frequency cluster, which was mainly active during the elastic shrinkage phase (Figure 6e). During the cavitation phase, however, the low- and mid-frequency clusters followed a very similar pattern and in the µCT experiment, we found a good correspondence between both low- and mid-frequency signals and visually observed cavitated vessels (Figure 7). The large number of empty vessels we found at the start of the µCT experiment mainly consisted of small primary vessels around the central pith (Vergeynst et al. 2015*a*). Jacobsen et al. (2015) performed active xylem staining experiments on *Vitis* samples, and concluded that bands of primary vessels around the pith become hydraulically inactive later on in the growing season. Nuclear magnetic resonance images of *Vitis* also showed similar results of empty primary vessels around the central pith before dehydration (Choat et al. 2010). Taking these inactive vessels into account has no repercussions on the sigmoidal shape of VCs, but when comparing different curves, initial vessel condition must be equal (e.g., all vessels filled or a fixed percentage empty). Finally, the correlation between visually observed cavitated vessels and low-frequency signals was slightly stronger than with mid-frequency signals. The higher number of mid-frequency AE signals causing the slightly weaker correlation during the initial dehydration phase (elastic shrinkage) compared with low-frequency signals may be explained by some overlap with the high-frequency cluster (discussed below).

Acoustic emission features support AE source identification

Besides AE activity, AE signal features (Figure 5) may also support identification of different AE sources in dehydrating branches. In

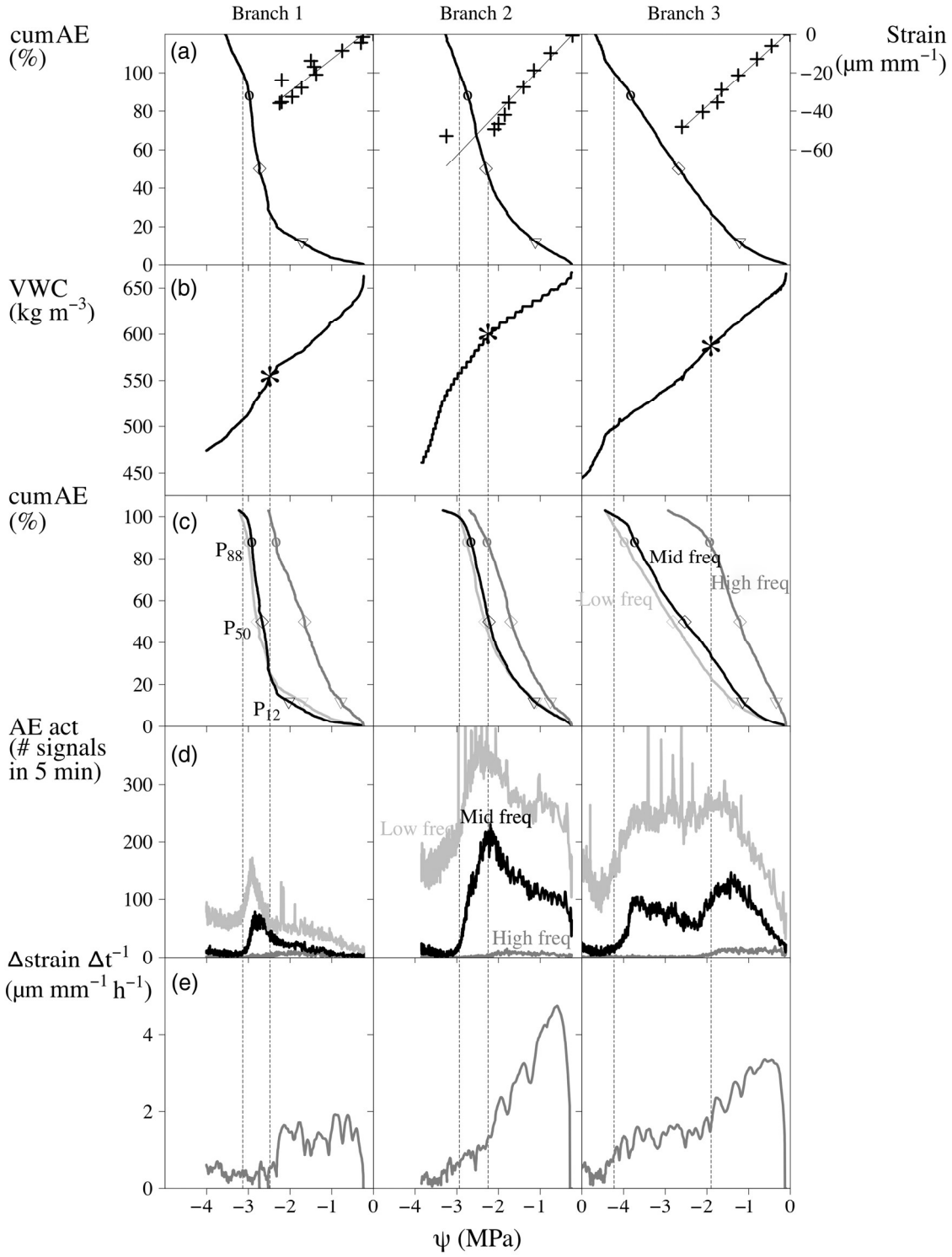

Figure 6. The left vertical dashed line indicates the end point of the VC of all AE signals (a). The transition between elastic shrinkage and cavitation phase based on changing hydraulic capacitance (b) is indicated by the right vertical dashed line. Based on the AE activity peak of the different signal types (d), we constructed three VCs (c) with P_{12}, P_{50} and P_{88} indicated by triangles, diamonds and circles, respectively. The shrinkage rate (Δ strain Δt^{-1}) was highest during the elastic shrinkage phase (e). The recorded spikes in the AE activity of Branches 2 and 3 are probably due to background noise and are therefore not completely shown.

general, AE signals are caused by sudden microscopic displacements, followed by damped vibration of the surfaces involved. These may include the surfaces of newly formed air bubbles in a xylem conduit as well as crack surfaces in or between the cell walls. The displacements are propagated away from the source as macroscopic elastic waves (pressure waves and shear waves), of

which the frequencies are influenced by the macroscopic elastic properties of the surrounding wood. When the initial displacement is large enough, and when the detector is sensitive for the propagated frequencies, a signal can be measured at the branch surface. The frequency content of the detected signal is related to the frequency spectrum of the source vibration (Sause and Horn 2010). We believe that the early activity of high-frequency AE signals (Figure 6d) resulted from two possible sources: (i) capillary action of free water and (ii) fast contraction of the bark during initial elastic shrinkage (Figure 6e). According to Tyree and Zimmermann (2002), capillary water is instantly released at the start of dehydration and, as illustrated by Tyree and Yang (1990), is accompanied by the production of AEs. Based on previous results obtained by Ogino et al. (1986), Rosner (2012) came to the conclusion that high-frequency components could be attributed to non-destructive capillary action of free water. Secondly, the bark of *Vitis* contains a proportion of dead cells and is known to easily peel off during dehydration. Kikuta (2003) examined AEs from different bark samples and concluded that certain dead elements (e.g., fibres) emit ultrasound AEs during dehydration. This type of signal, containing high frequencies, with relatively high peak amplitude, short rise time and thus large rise angle (Figure 5), has also been related to surface checking in drying oak (*Quercus variabilis* Blume) (Kim et al. 2005). Signals originate from very fast movements of the microscopic fracture surfaces or micro-cracks in or between cell walls (Čunderlik et al. 1996) being pulled apart. In the field of fracture mechanics, this is called tensile cracking (Aggelis et al. 2010). However, as illustrated by Yamamoto et al. (2013), micro-crack formation occurs when the moisture content decreases below fibre saturation point. Thus, discussion about whether these micro-cracks contribute to the high-frequency AE signals at the start of dehydration remains and further research is necessary. Note that the high-frequency AE signals decrease to a minimum at the start of the cavitation phase (Figure 6d), which can be explained by bark shrinkage reaching its end point.

The formation of macro-cracks is associated with shear stresses, and so-called shear cracking is accompanied by AE signals with high energy, a long rise time and low frequencies (Aggelis et al. 2010), comparable to the low-frequency cluster that we observed (Figure 5). Beyond 100% PLC, when tension in the xylem conduits is released by cavitation, the stress field changes and existing fractures may grow by shear stresses leading to strong low-frequency signals. However, we distinguish a second possible origin for the low-frequency signals beyond 100% PLC. At the moment when all hydraulic conductivity is lost, the VWC is still far above the fibre saturation point. Free water that is still left in the wood, and which is disconnected from the transpiration stream, may move under influence of a combination of viscous, capillary and gravity forces (Løvoll et al. 2005). The movement of the drainage front through a porous medium is characterized by rapid meniscus displacements, called Haines jumps (Haines 1930). These rapid rearrangements of the air–water interfaces have been related to AE signals in the frequency range 50–250 kHz (Chotard et al. 2007), 10–30 kHz and below 3.75 kHz (DiCarlo et al. 2003), and could occur, e.g., when a

Table 2. Parameters derived from the dehydration curves: apparent radial modulus of elasticity (E_r') (Figure 6a), water potential at transition point between shrinkage and cavitation phase (Figure 6b) and hydraulic capacitance (C) for both phases.

	E_r' (MPa)	Transition point (MPa)	C (kg m^{-3} MPa^{-1})	
			Shrinkage phase	Cavitation phase
Branch 1	59.1	–2.48	39.1	73.3
Branch 2	44.2	–2.25	30.4	59.5
Branch 3	51.0	–1.90	37.7	36.2

Table 3. Characteristic water potential values of the VCs using all AE signals (Figure 6a), compared with the three clusters (low-, mid- and high-frequency) of AE signals (Figure 6c). The cumulative number of AE signals at 100% PLC ($cumAE_{100}$) is indicated for each curve.

	P_{12} (MPa)	P_{50} (MPa)	P_{88} (MPa)	P_{100} (MPa)	$cumAE_{100}$ ($\times 10^3$ signals)
Branch 1					
All signals	–1.71	–2.73	–2.98	–3.13	95
Low-frequency	–1.71	–2.78	–3.01	–3.17	65
Mid-frequency	–2.03	–2.67	–2.92	–3.06	26
High-frequency	–0.78	–1.65	–2.33	–2.48	2
Branch 2					
All signals	–1.12	–2.30	–2.74	–2.94	186
Low-frequency	–1.09	–2.32	–2.77	–2.93	125
Mid-frequency	–1.14	–2.23	–2.66	–2.96	54
High-frequency	–0.76	–1.70	–2.28	–2.56	2
Branch 3					
All signals	–1.22	–2.68	–3.83	–4.23	183
Low-frequency	–1.37	–2.81	–3.98	–4.35	139
Mid-frequency	–1.15	–2.53	–3.74	–4.17	43
High-frequency	–0.34	–1.21	–1.93	–2.62	2

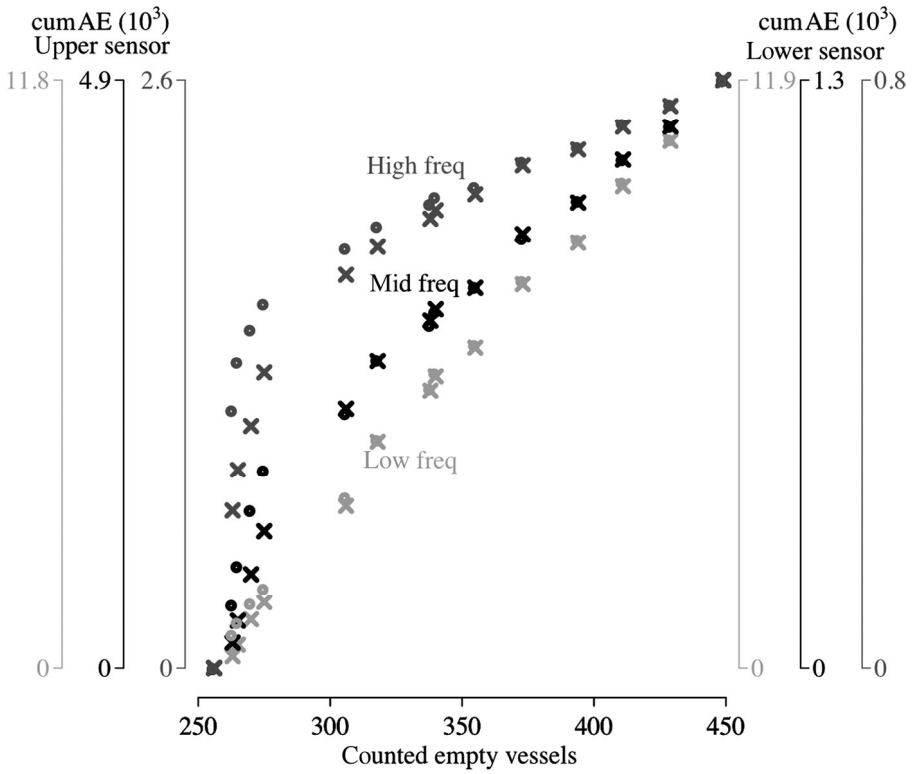

Figure 7. The cumulative number of AEs was most related with visual observation of cavitation for the mid- and low-frequency clusters. The high-frequency cluster showed a proportionally higher activity in the beginning of the dehydration experiment. The dehydration experiment in the µCT scanner lasted for 40 h and the experiment was stopped before the end point of the cavitation phase was reached (Vergeynst et al. 2015*a*).

meniscus passes a perforation plate of a xylem vessel. Also during the cavitation phase, movement of water that was disconnected from the transpiration stream by gas emboli may result in these low-frequency signals. This may explain the high activity of low-frequency signals with a similar pattern to the mid-frequency signals during the cavitation phase (Figure 6d).

The formation of a gas bubble (Vincent et al. 2012, 2014) in a xylem conduit under tension is most probably a more violent event than drainage of free water because of the large pressure drop involved. Faster movements at the AE sources result in higher frequencies, explaining the higher frequencies of the mid-frequency cluster related to cavitation. Vincent et al. (2014) found that the bubble vibration frequency is inversely proportional to the bubble radius. This might result in a certain frequency range of cavitation-induced AE signals, dependent on the bubble size. However, the total number of AE signals in the mid-frequency cluster (Table 3) exceeds the number of xylem vessels that might be expected in a 36-cm-long branch (Vergeynst et al. 2015*a*) by one or two orders of magnitude. On the one hand, the boundaries of this cluster, obtained with the clustering algorithm, might be too wide and might include signals that belong to one of the other AE sources. On the other hand, with the current limited mechanistic understanding of the cavitation process (Rockwell et al. 2014) in angiosperms, it is not self-evident that one embolized conduit results from the birth of one air bubble. The nanobubble theory (Schenk et al. 2015) states that many nanobubbles could be formed in the xylem sap before they coalesce to form an obstructing air bubble. The AEs due to nanobubble formation might explain the large number of cavitation-related AE signals. Eventually, bubble collapse in the pit chamber may produce AE signals without resulting in the embolization of a conduit.

Differences, but also overlap, between clusters due to wave propagation

Although only the mid-frequency cluster complied with the features expected upon the occurrence of cavitation, the shape of the VC (Figure 6c) and calculated P_{50} (Table 3) were very close when either the low- or mid-frequency cluster was used. Moreover, the correlation between low-frequency signals and visually observed cavitation (Figure 7) was even better than for mid-frequency signals. The main reason for this slight deviation in pattern of the mid-frequency cluster is probably the overlap between clusters caused by wave propagation. The bulk of the AE signals has propagated some distance along the branch before reaching the sensor, which gives rise to guided waves. Differences in source location (Vergeynst et al. 2015*b*) may influence the frequency content and thus the location in the scatterplots (Figure 4). Therefore, a particular AE source results in a point cloud, which may show some overlap with adjacent point

clouds. Moreover, in wood, higher frequencies are attenuated more strongly than lower frequencies (Beall 2002), and attenuation decreases strongly with ongoing dehydration (Vergeynst et al. 2015*b*). Acoustic emission sources of higher frequency may thus fall into a lower-frequency cluster due to a frequency shift by attenuation. Part of the activity of the mid-frequency cluster during the initial elastic shrinkage phase thus probably resulted from high-frequency AE sources, related to shrinkage at a longer distance from the detector. This could result in a risk of overestimating PLC at low tensions (Figure 7). For this reason, Beall (2002) already suggested using an upper frequency level of 100–200 kHz for transducers on woody material. In the same way, part of the low-frequency signals during the cavitation phase could be explained by overlap with the mid-frequency cluster, resulting in similar VC features (Figure 6c). However, Haines jumps during drainage of water after tension release by cavitation form a plausible cause of cavitation-related low-frequency signals, explaining the good correspondence with visually observed cavitation (Figure 7) and valid VC curves (Figure 6c). To reduce the overlap between AE signal clusters, source localization would be helpful to account for frequency changes due to attenuation.

In general, even when no distinction would have been made between different AE sources (Figure 6a), the VC parameters (Table 3) did not change substantially compared with the filtered mid-frequency VC in our experiment. We explain this by the very low activity of high-frequency AE sources during elastic shrinkage, and a relatively constant or simultaneous activity of the low-frequency AE sources during the cavitation phase. However, when measuring on other branches, other species and in different environments, the coordination between the different AE sources might change, necessitating the filtering of specific cavitation-induced AE signals as proposed in this article. It is therefore recommended to use the broadband sensor in future research. The possibility to distinguish between different AE sources, and to link them to specific physiological processes, is a major breakthrough in the use of AE monitoring in cavitation research. However, when it is sufficiently demonstrated that the resonant sensor shows good results, its use might be preferred in further practical applications. This clustering approach also has great potential to detect non-destructive cavitation in the field by considering only mid-frequency signals. This would be of great use to clarify the current controversy about diurnal emboli formation and repair (Sperry 2013).

Conclusion

Three clusters of AE signals were active during the dehydration of grapevine branches. Based on differences in AE features and AE activities during consecutive dehydration phases, we concluded that the mid-frequency signal type was most related to cavitation. High-frequency signals probably resulted from capillary action of free water and fast contraction of the bark during elastic shrinkage, while low-frequency signals were most likely caused by macro-fractures or Haines jumps. In our experiment, the filtered VC based on mid-frequency signals did not strongly differ from the curve based on total AE activity. However, for reliable widespread application of the AE technique, and for in vivo measurements, more fundamental research is necessary to elucidate the AE-inducing processes during cavitation. To this end, distinction between the different types of AE signals is imperative. Moreover, the information contained in the AE signals should be used as a precious resource to support important ongoing discussions on the processes behind hydraulic failure.

Acknowledgments

The authors are grateful to H. Jochen Schenk for the fruitful discussion on Haines jumps in porous media and to Bart Vanryckegem for providing plant material.

Conflict of interest

None declared.

Funding

This work was supported by the Research Foundation – Flanders (FWO) (Ph.D. funding granted to L.L.V. and the research programme G.0941.15N granted to K.S.) and the Commission for Scientific Research (Faculty of Bioscience Engineering, Ghent University).

References

Adler D (2005) vioplot: Violin plot. R package version 0.2. https://cran.r-project.org/web/packages/vioplot (7 April 2016, date last accessed).

Aggelis DG, Matikas TE, Shiotani T (2010) Advanced acoustic techniques for health monitoring of concrete structures. In: Kim SH, Ann KY (eds) The Song's handbook of concrete durability. Middleton Publishing Inc., Seoul, Korea, pp 331–378.

Aggelis DG, Barkoula N-M, Matikas TE, Paipetis AS (2013) Acoustic emission as a tool for damage identification and characterization in glass reinforced cross ply laminates. Appl Compos Mater 20:489–503.

Baensch F, Sause MGR, Brunner AJ, Niemz P (2015) Damage evolution in wood—pattern recognition based on acoustic emission (AE) frequency spectra. Holzforschung 69:357–365.

Beall FC (2002) Overview of the use of ultrasonic technologies in research on wood properties. Wood Sci Technol 36:197–212.

Brodersen CR, McElrone AJ, Choat B, Lee EF, Shackel KA, Matthews MA (2013) In vivo visualizations of drought-induced embolism spread in *Vitis vinifera*. Plant Physiol 161:1820–1829.

Carevic F, Fernández M, Alejano R, Vázquez-Piqué J (2014) Xylem cavitation affects the recovery of plant water status and consequently acorn production in a holm oak open woodland. Acta Physiol Plant 36:3283–3290.

Choat B, Drayton WM, Brodersen CR, Matthews MA, Shackel KA, Wada H, McElrone AJ (2010) Measurement of vulnerability to water

stress-induced cavitation in grapevine: a comparison of four techniques applied to a long-vesseled species. Plant Cell Environ 33:1502–1512.
Chotard T, Smith A, Quet A (2007) Characterisation of liquid transfer processes and water adsorption mechanism on a porous ceramic by acoustic emission means. J Eur Ceram Soc 27:457–462.
Cochard H, Badel E, Herbette S, Delzon S, Choat B, Jansen S (2013) Methods for measuring plant vulnerability to cavitation: a critical review. J Exp Bot 64:4779–4791.
Čunderlik I, Molinski W, Raczkowski J (1996) The monitoring of drying cracks in the tension and opposite wood by acoustic emission and scanning electron microscopy methods. Holzforschung 50:258–262.
Delzon S, Cochard H (2014) Recent advances in tree hydraulics highlight the ecological significance of the hydraulic safety margin. New Phytol 203:355–358.
DiCarlo DA, Cidoncha JIG, Hickey C (2003) Acoustic measurements of pore-scale displacements. Geophys Res Lett 30:1901. doi:10.1029/2003GL017811
Haines WB (1930) Studies in the physical properties of soil. V. The hysteresis effect in capillary properties, and the modes of moisture distribution associated therewith. J Agric Sci 20:97–116.
Irvine J, Grace J (1997) Continuous measurements of water tensions in the xylem of trees based on the elastic properties of wood. Planta 202:455–461.
Jacobsen AL, Rodriguez-Zaccaro FD, Lee TF, Valdorinos J, Toschi HS, Martinez JA, Pratt RB (2015) Grapevine xylem development, architecture and function. In: Hacke UG (ed) Functional and ecological xylem anatomy. Springer, pp 133–162.
Kikuta SB (2003) Ultrasound acoustic emissions from bark samples differing in anatomical characteristics. Phyton 43:161–178.
Kim KB, Kang HY, Yoon DJ, Choi MY (2005) Pattern classification of acoustic emission signals during wood drying by principal component analysis and artificial neural network. Mater Sci Eng 297–300: 1962–1967.
Lens F, Tixier A, Cochard H, Sperry JS, Jansen S, Herbette S (2013) Embolism resistance as a key mechanism to understand adaptive plant strategies. Curr Opin Plant Biol 16:287–292.
Løvoll G, Méheust Y, Måløy K, Aker E, Schmittbuhl J (2005) Competition of gravity, capillary and viscous forces during drainage in a two-dimensional porous medium, a pore scale study. Energy 30:861–872.
Martin-StPaul NK, Longepierre D, Huc R, Delzon S, Burlett R, Joffre R, Rambal S, Cochard H (2014) How reliable are methods to assess xylem vulnerability to cavitation? The issue of 'open vessel' artifact in oaks. Tree Physiol 34:894–905.
McElrone AJ, Brodersen CR, Alsina MM, Drayton WM, Matthews MA, Shackel KA, Wada H, Zufferey V, Choat B (2012) Centrifuge technique consistently overestimates vulnerability to water stress-induced cavitation in grapevines as confirmed with high-resolution computed tomography. New Phytol 196:661–665.
Nolf M, Beikircher B, Rosner S, Nolf A, Mayr S (2015) Xylem cavitation resistance can be estimated based on time-dependent rate of acoustic emissions. New Phytol 208:625–632.
Ogino S, Kaino K, Suzuki M (1986) Prediction of lumber checking during drying by means of acoustic emission technique. J Acoust Emiss 5:61–65.
Ponomarenko A, Vincent O, Pietriga A, Cochard H, Badel E, Marmottant P (2014) Ultrasonic emissions reveal individual cavitation bubbles in water-stressed wood. J R Soc Interface 11:20140480. doi:10.1098/rsif.2014.0480
R Development Core Team (2013) R: a language and environment for statistical computing. The R Foundation for Statistical Computing, Vienna, Austria, ISBN 3-900051-07-0. http://www.R-project.org (7 April 2016, date last accessed).
Rockwell FE, Wheeler JK, Holbrook NM (2014) Cavitation and its discontents: opportunities for resolving current controversies. Plant Physiol 164:1649–1660.
Rosner S (2012) Waveform features of acoustic emission provide information about reversible and irreversible processes during spruce sapwood drying. Bioresources 7:1253–1263.
Rosner S (2015) A new type of vulnerability curve: is there truth in vine? Tree Physiol 35:410–414.
Rosner S, Klein A, Wimmer R, Karlsson B (2006) Extraction of features from ultrasound acoustic emissions: a tool to assess the hydraulic vulnerability of Norway spruce trunkwood? New Phytol 171:105–116.
Sause MGR (2010) Identification of failure mechanisms in hybrid materials utilizing pattern recognition techniques applied to acoustic emission signals. Ph.D. thesis, Universität Augsburg, Mensch und Buch, Germany, 305 p.
Sause MGR, Horn S (2010) Simulation of acoustic emission in planar carbon fiber reinforced plastic specimens. J Nondestruct Eval 29:123–142.
Sause MGR, Gribov A, Unwin AR, Horn S (2012*a*) Pattern recognition approach to identify natural clusters of acoustic emission signals. Pattern Recogn Lett 33:17–23.
Sause MGR, Hamstad MA, Horn S (2012*b*) Finite element modeling of conical acoustic emission sensors and corresponding experiments. Sensor Actuator A Phys 184:64–71.
Schenk HJ, Steppe K, Jansen S (2015) Nanobubbles: a new paradigm for air-seeding in xylem. Trends Plant Sci 20:199–205.
Sperry J (2013) Cutting-edge research or cutting-edge artefact? An overdue control experiment complicates the xylem refilling story. Plant Cell Environ 36:1916–1918.
Torres-Ruiz JM, Jansen S, Choat B et al. (2015) Direct X-ray microtomography observation confirms the induction of embolism upon xylem cutting under tension. Plant Physiol 167:40–43.
Tyree MT, Dixon MA (1983) Cavitation events in *Thuja occidentalis* L.? Ultrasonic acoustic emissions from the sapwood can be measured. Plant Physiol 72:1094–1099.
Tyree MT, Yang S (1990) Water-storage capacity of *Thuja*, *Tsuga* and *Acer* stems measured by dehydration isotherms. Planta 182:420–426.
Tyree MT, Zimmermann MH (2002) Xylem structure and the ascent of sap, 2nd edn. Springer, Berlin, Germany, 283 p.
Vergeynst LL, Dierick M, Bogaerts JAN, Cnudde V, Steppe K (2015*a*) Cavitation: a blessing in disguise? New method to establish vulnerability curves and assess hydraulic capacitance of woody tissues. Tree Physiol 35:400–409.
Vergeynst LL, Sause MGR, Hamstad MA, Steppe K (2015*b*) Deciphering acoustic emission signals in drought stressed branches: the missing link between source and sensor. Front Plant Sci 6:494. doi:10.3389/fpls.2015.00494
Vincent O, Marmottant P, Quinto-Su PA, Ohl C-D (2012) Birth and growth of cavitation bubbles within water under tension confined in a simple synthetic tree. Phys Rev Lett 108:184502. doi:10.1103/PhysRevLett.108.184502
Vincent O, Marmottant P, Gonzalez-Avila SR, Ando K, Ohl C-D (2014) The fast dynamics of cavitation bubbles within water confined in elastic solids. Soft Matter 10:1455–1461.
Wolkerstorfer SV, Rosner S, Hietz P (2012) An improved method and data analysis for ultrasound acoustic emissions and xylem vulnerability in conifer wood. Physiol Plant 146:184–191.
Yamamoto H, Sakagami H, Kijidani Y, Matsumura J (2013) Dependence of micro-crack behavior in wood on moisture content during drying. Adv Mater Sci Eng 2013:1–7.